CrossMark

Single image super resolution for texture images through neighbor embedding

**Deepasikha Mishra[1] · Banshidhar Majhi[1] ·
Sambit Bakshi[1]** 🄳 **· Arun Kumar Sangaiah[2] ·
Pankaj Kumar Sa[1]**

Abstract This article proposes an improved learning based super resolution scheme using manifold learning for texture images. Pseudo Zernike moment (PZM) has been employed to extract features from the texture images. In order to efficiently retrieve similar patches from the training patches, feature similarity index matrix (FSIM) has been used. Subsequently, for reconstruction of the high resolution (HR) patch, a collaborative optimal weight is generated from the least square (LS) and non-negative matrix factorization (NMF) methods. The proposed method is tested on some color texture, gray texture, and some standard images. Results of the proposed method on texture images advocate its superior performance over established state-of-the-art methods.

Keywords Super resolution · Manifold learning · Pseudo Zernike moment · Feature similarity index

---

✉ Sambit Bakshi
  bakshisambit@nitrkl.ac.in; sambitbaksi@gmail.com

  Deepasikha Mishra
  deepasikhame@gmail.com

  Banshidhar Majhi
  bmajhi@nitrkl.ac.in

  Arun Kumar Sangaiah
  sarunkumar@vit.ac.in; arunkumarsangaiah@gmail.com

  Pankaj Kumar Sa
  pankajksa@nitrkl.ac.in; pankajksa@gmail.com

[1]   Department of Computer Science and Engineering, National Institute of Technology,
    Rourkela, Odisha - 769 008, India

[2]   School of Computing Science and Engineering, Vellore Institute of Technology, Vellore,
    Tamil Nadu - 632 014, India

🖄 Springer

1 Introduction

Image analysis is a universal need in image processing and computer vision. However, lack of high-frequency details in an image leads to incorrect image analysis. To overcome such issues, super resolution (SR) technique has been used to generate a high resolution (HR) image from the given low resolution (LR) image(s) observations [23]. Prior to SR algorithm, another possible approach was adopted to increase the number of pixels per unit area to combat the loss of high-frequency details. Such process considers the decrease in pixel size and increases the number of sensors [36–38]. However, due to diffraction effect decreasing the pixel size prompts to high capacitance which in turn slows down the system performance and results in increase of noise. SR algorithm is devoid of such limitations and found to be suitable in applications like satellite and areal imaging, medical image processing, textured recognition, face recognition, video surveillance, etc.

Various research articles have been reported on SR techniques over the past two decades. Generally, the SR can be achieved on both frequency as well as spatial domain [2, 18, 30, 35, 45]. Furthermore, the SR methods can be broadly categorized into two types such as (i) Multi frame SR and (ii) Single frame SR based on the number of LR reference images considered. Various multi image based SR approaches [21, 28, 38, 41] require accurate registration among images which lead to ringing effects and artifacts in the reconstructed image. In addition, they do not work well for unprocessed data. On the other hand, single image LR image based SR methods do not suffer from these problems. Further, existing single image based SR approaches can be classified into three general classes, i.e., interpolation based, reconstruction based and learning based. In the interpolation based methods [29, 51], it is hard to restore the high-frequency details. Therefore, blurred edge and complex texture are found in interpolation method. In reconstruction based method [30, 54], prior knowledge like edge, gradient, etc. are required to reconstruct the HR image. This method can suppress the aliasing artifacts and preserve sharper edges. However, it cannot generate fine details in larger magnification. To tackle this problem, learning based SR methods [5, 7, 9, 20, 52] have been introduced by inferring the mapping relationship between LR-HR image pairs.

Learning based SR approach can be further categorized into three categories such as belief network [3, 19, 20], manifold learning [6, 7, 9, 13] and compressive sensing [46, 47, 50]. Freeman et al. [19] are the forerunners who introduced learning based single image super resolution scheme in 1999. Later on, they have used Markov random field (MRF) model and loopy belief propagation to find the relationship between LR-HR image patch pairs. However, boundary effect and incompatibility between reconstructed HR patches and its surrounding patches have been seen in texture images [19, 20]. Based on these works, Sun et al. [40] proposed primal sketch apriori to overcome the blur present in edges, ridges and corners. To overcome the incompatibility between HR patches and its neighboring patches, manifold learning based super resolution techniques have been introduced in [4, 5, 7, 9]. Chang et al. [9] introduced single image SR using manifold learning where local geometry based features are extended from LR-HR patch pairs inferred to reconstruct the expected HR patches using optimal reconstruction weight. Thereafter, a novel feature selection scheme for neighbor embedding SR has been proposed by Chan et al. [7]. Guo et al. [24] have used maximum a posteriori (MAP) estimation to combine the global parametric constraint with a patch-based local non-parametric constraint. In another work, Gao et al. [22] have proposed a method to project the original HR and LR patch onto the jointly learning unified feature subspace. Later on, compressive sensing techniques have drawn attention from many researchers for single image super resolution [16, 26]. Mishra

et al. [33] have introduced a robust scheme to generate a HR image from the registered LR image. In this work,they remove the outlier generated during registration using robust locally linear embedding (RLLE). Further, they used Zernike moment as feature selection for neighborhood preservation during HR image reconstruction [34].

In addition to these, few other studies have also proposed for the enhancement of texture image. Wei et al. [44] have discussed the extensions and applications of texture synthesis. HaCohen et al. [25] introduced consistent fine-scale detail to textured regions and produced edges with proper sharpness. To enhance the quality of complicated texture structure in the image, an example based SR using clustering and partially supervised neighbor embedding has been proposed by Zhang et al. [52]. Due to overlapping in the frequency range with that of the noise in the texture images, de-noising or in-painting is used for single image super resolution [49]. Yoo et al. [48] proposed a novel texture enhancement strategy to improve the single image super resolution performance. In recent years, many neural network (NN) based approaches has addressed for single image super resolution with excellent performance. Ahn et al. [1] proposed a texture enhancement framework by the combining interpolation technique and customized style transfer technique. Here they used repetitive tiling concept for the style transfer technique. Sajjadi et al. [39] introduced an automated texture synthesis technique by using feed forward fully convolutional neural networks. This method gives an efficient result due to the feed-forward architecture which inference time since the LR image only needs to be passed through the network once to get the result. Liu et al. [31] used total variation (TV) regularization approach for SR image reconstruction for synthetic aperture radar (SAR) image. In this work, they used gradient profile prior or other texture image prior in the maximum a posteriori framework. Cruz et al. [15] used Wiener filter in similarity domain to generate a super resolution image from a single reference image. Here they introduced filtering of the patches in 1D similarity domain and coupled it with the iterative back propagation (IBP) frame work. Chang et al. [11] presented a bi-level semantic representation analysing framework for image/ video which is work for weight learning approach for multimedia representation. Later, they introduced a semi supervised feature selection technique. For maintain the correlation between various feature in the training data they adopted manifold learning to labeled and unlabelled training data [8]. In addition, to maintain the correlation between the linear effect and the nonlinear effect for embedding feature interaction, an optimization algorithm has been proposed by them [10]. An isotonic regularizer that is able to exploit the constructed semantic ordering information has introduced by Chang et al. [12] for the video shots.

The literature review reveals that most of the existing schemes fail to reproduce the fine details during image reconstruction. Different applications on SR need suitable algorithms in order to achieve an optimal reconstruction image. Enhancement in texture images still points as an outstanding problem. In this work, we propose an improved learning based SR algorithm for texture image to generate a HR image from a single LR image. The scheme utilizes neighbor embedding technique (manifold learning) and is suitably named as single image super resolution using manifold learning (SSRM). In this approach, HR patches are reconstructed from the input test LR patches by the prior information that fetched from the training LR-HR pairs. The major contribution of this paper includes

1. Feature representation using pseudo Zernike moments (PZM) to classify the patches
2. Finding the k most similar patches from the test patch using similarity measure, i.e. Feature similarity index (FSIM)

3. Computation of optimal reconstruction weight using least square (LS) and non-negative matrix factorization (NMF) for HR patch reconstruction

Experimental results and comparisons on textural images show that proposed method offers better performance than other existing methods. Additionally, the proposed scheme works well on standard images.

The rest of the paper is organized as follows. Section 2 discusses the proposed algorithm. The experimental results and discussion are presented in Section 3. Finally, Section 4 deals with the concluding remarks and the scope for future work.

2 Proposed SSRM algorithm

In this work, an improved single image SR using manifold learning is proposed. The scheme follows three main steps

 (i)   feature extraction using pseudo Zernike moments (PZM)
 (ii) finding k-nearest neighbor using similarity measure FSIM
 (iii) optimal reconstruction weight computation using collaborative method

Features are extracted from each LR-HR patch separately by considering the phase and magnitude values of PZM. In addition, FSIM has been used as a similarity measure for searching the nearest neighbor patches for HR patch reconstruction. Thereafter, a collaborative technique is used to find out the optimal reconstruction weight to generate the HR patch from a given LR input patch. Figure 1 shows the overall frame work of the proposed scheme.
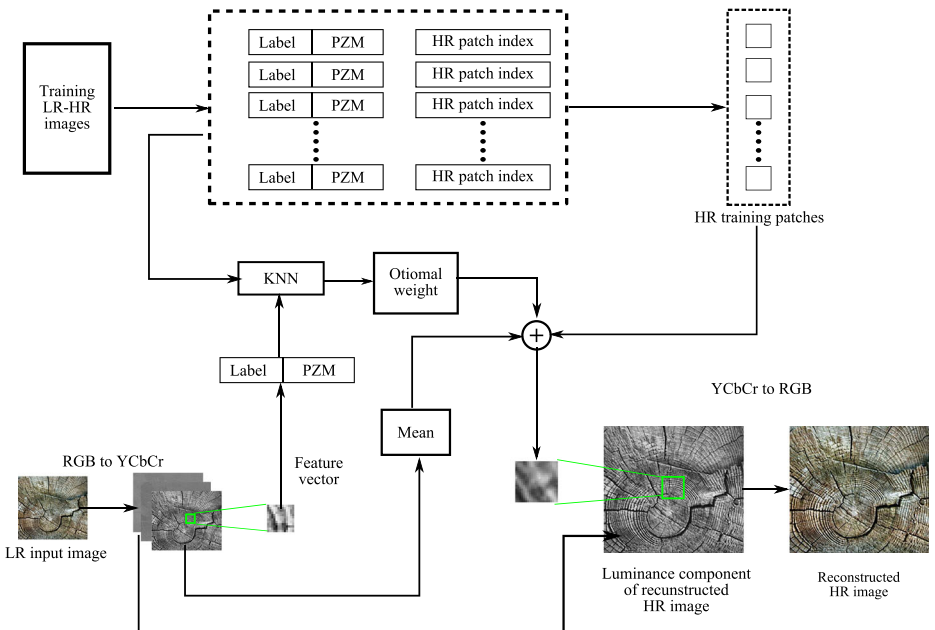

Fig. 1 Overall block diagram of proposed scheme

The overall steps to generate the reconstructed HR image is listed in Algorithm 1.

Algorithm 1 Proposed Super resolution through neighbor embedding

---

Require: Training HR image $H_r = \{h_r^p\}_{p=1}^a$ and its corresponding LR image $L_r = \{l_r^p\}_{p=1}^a$, LR input image $L_t = \{l_t^q\}_{q=1}^b$ as testing image, Magnification factor γ and patch size t.

Ensure: Targeted HR image H_t.

  1: Split L_t and L_r into patches of $t \times t$ with overlapping by 2 pixels.
  2: Split H_r into patches of $\gamma t \times \gamma t$ with overlapping by 2γ pixels.
  3: Generate feature vector using PZM .
  4: **for** each patch $l_t^q \epsilon L_t$. **do**
  5:     Compute k-nearest neighbors set $\aleph_q$ among all patches using feature similarities index.
  6:     Compute optimal reconstruction weight vector w_{ql}.
  7:     Compute targeted HR patch h_t^q.
  8: **end for**
  9: Merge all h_t^q to get luminance component of targeted HR image H_t by enforcing inter-patch relationships.

2.1 Patch generation

In this approach, each image is first converted from RGB to $YCbCr$ color model and only the luminance component of the image is considered. Each LR image is decomposed into a set of $t \times t$ patches with two overlapping pixels. The corresponding HR image patch size is $\gamma t \times \gamma t$ with 2γ overlapping pixels, where γ is the magnification factor. Let the training LR image, HR image and testing LR image are denoted by $L_r = \{l_r^p\}_{p=1}^a$, $H_r = \{h_r^p\}_{p=1}^a$, and $L_t = \{l_t^q\}_{q=1}^b$, respectively. The number of patches for the LR image of size $t \times t$ is $t \times t \times [(row - stepsize) \times (col - stepsize)]$, where $stepsize = patchsize - overlappingpixels$. The number of patches for the HR image of size $\gamma t \times \gamma t$ is $\gamma t \times \gamma t \times [(row - stepsize) \times (col - stepsize)]$, where $stepsize = \gamma \times patchsize - \gamma \times overlappingpixels$.

2.2 Feature selection by PZM

In this work, we use pseudo Zernike moment (PZM) for feature selection. It has higher description ability for same order as compared to Zernike moment. Moreover, it provides meaningful information for image reconstruction. It is a widely used orthogonal moment. It has several applications in various areas of image processing and pattern recognition. Because of its orthogonality and invariance properties, it is robust to noise and have better ability for image representation [14]. Figure 2 shows the linear transformation on a single patch through normalization.

The PZM of a continous image intensity $f(x, y)$ is defined as

$$PZM_{n,m}(f(x, y)) = \frac{n+1}{\pi} \int \int_{x^2+y^2 \leq 1} f(x, y) V_{n,m}^*(x, y) \, dxdy, \qquad (1)$$
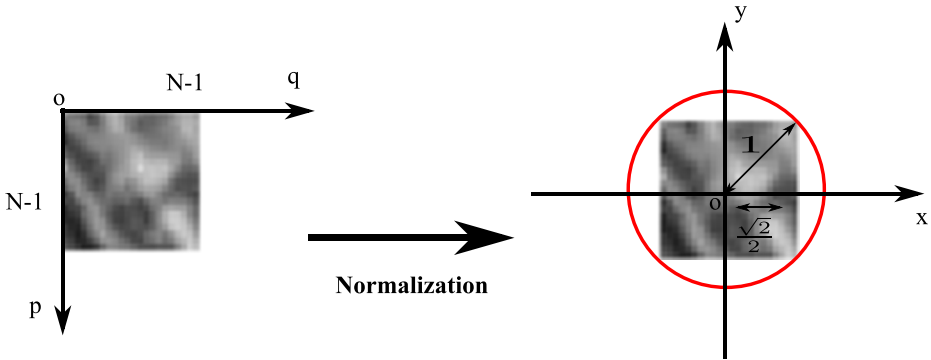
Fig. 2 Normalization of the patch in unit circle

where n, m is the order and repetition respectively. Here, $n = 0, 1, 2, ..., \infty$ and $|m| \leq n$ such that $n - |m| = even$. The discrete form of PZM for digital image intensity $f(x_q, y_p)$ is represented as

$$PZM_{n,m}\left(f\left(x_q, y_p\right)\right) = \frac{n+1}{\pi\lambda(N)} \sum_x \sum_y V_{n,m}^*(x, y)\left(f\left(x_q, y_p\right)\right), \qquad (2)$$

where $x_q = -\frac{\sqrt{2}}{2} + \frac{\sqrt{2}}{N-1}q$, $q = 0, 1, .., (N-1)$ and $y_p = \frac{\sqrt{2}}{2} - \frac{\sqrt{2}}{N-1}p$, $p = 0, 1, .., (N-1)$. Here $\frac{n+1}{\pi}$ is a normalization factor, $\lambda(N) = \frac{N^2}{2}$. $V_{n,m}$ is the complex polynomial and $V_{n,m}^*$ is the complex conjugate of $V_{n,m}$.

The pseudo Zernike polynomials is represented as

$$V_{n,m}(x, y) = R_{n,m}(r)\, e^{jm\theta}, \qquad (3)$$

where radial polynomials $R_{n,m}(r)$ is defined as

$$R_{n,m}(r) = \sum_{s=0}^{n-|m|} (-1)^s \frac{(2n+1-s)!}{s!(n-|m|-s)!(n+|m|+1-s)!} r^{(n-s)}, \qquad (4)$$

here the PZM are defined in terms of polar coordinates (r, θ) with $0 \leq |m| \leq n$ and $|r| \leq 1$.

It is reported that PZM is unsuitable to extract the global information from the whole image. Hence, in this scheme, we compute the feature vector for each patch with respect to magnitude and phase of PZM [27].

2.2.1 Generation of feature vector considering the magnitude of the PZM

Generally, the 2-D PZM feature is represented by a complex value, which is the combination of magnitude and phase coefficients. The magnitude based PZM feature vector of order $n = 0$ to n_{max}, with $m \geq 0$ is represented in Table 1. For $n_{max} = 5$, the total number of feature vector is 21. Since, PZM with higher order moment is sensitive to noise and distortion, we consider 5 as the maximum order. So the feature vector for each patch $f(x_q, y_p)$ is defined as

$$PZM^{n_{max}}\left[f(x_q, y_p)\right] = \left\{|PZM_{u,v}(f(x_q, y_q))||, u = 0, 1, ..., n_{max}, v = o, i, ..., u\right\}, \quad (5)$$

where $|PZM_{u,v}(f(x_q, y_q))|$ is the magnitude of $PZM_{n,m}(f(x_q, y_p))$.

Table 1 PZM with n=0 to 5

n	PZM	No. of PZM
0	$PZM_{0,0}$	1
1	$PZM_{1,0}, PZM_{1,1}$	2
2	$PZM_{2,0}, PZM_{2,1}, PZM_{2,2}$	3
3	$PZM_{3,0}, PZM_{3,1}, PZM_{3,2}, PZM_{3,3}$	4
4	$PZM_{4,0}, PZM_{4,1}, PZM_{4,2}, PZM_{4,3}, PZM_{4,4}$	5
5	$PZM_{5,0}, PZM_{5,1}, PZM_{5,2}, PZM_{5,3}, PZM_{5,4}, PZM_{5,5}$	6

2.2.2 Generation of feature vector considering the phase of the PZM

The wide range of edges are represented by high phase values. The gradient based edge detection technique are sensitive to blurring and magnification. Hence, in this work, PZM is used to preserve the high-frequency details during image reconstruction. By using various heuristic criteria, the patch with edge and without edge can be calculated from the training patches. Hence, for a input test patches, it will be easy to classify the nearest neighbor patches from the whole training patch. Then each patch having edge is counted according to Table 2. It will speed-up the searching process. In order to compute the phase feature, rotation invariant PZM is defined as

$$\left| PZM_{n,m}^{R}(f(x_q, y_p)) \right| = \left| PZM_{n,m}(f(x_q, y_p)) \right| \exp^{-jm\theta}, \tag{6}$$

where $PZM_{n,m}^{R}(f(x_q, y_p))$ is the rotated version of PZM with the rotation angle θ. To remove the rotational effect on phase, a complex valued rotation invariant is created by combining phase coefficients of different orders with repetitions. This is represented as

$$\widehat{PZM_{n,m}}(f(x_q, y_p)) = PZM_{n,m}(f(x_q, y_p))\exp^{-jm\varphi_{n_0,1}}, n_0 = 1, ..., n_{\max}, \tag{7}$$

where $\varphi_{n,m}^{R} = \varphi_{n,m} - m\theta$. Here, $\varphi_{n,m}$ the phase coefficient and $\varphi_{n,m}^{R}$ is the phase value of rotated image. When we set $n_0 = 1$ the modified phase angle of PZM is

$$\widehat{\varphi_{n,m}} = \varphi_{n,m} - m\varphi_{1,1}, \tag{8}$$

where $\varphi_{1,1} = 0$. Therefore, the phase feature vector of each patch $f(x_q, y_p)$ is represented as

$$\overset{n_{max}}{\widehat{\varphi}} \left[f(x_q, y_p) \right] = \left\{ |\widehat{\varphi_{u,v}}(f(x_q, y_p))\| u = 1, 2, ..., n_{max}, v = 1, ..., u, \text{except} : (u = 1, v = 1) \right\}. \tag{9}$$

After the phase feature vector generation, several heuristic criteria have been used for identify the patches with edge and without edge. If $\phi < \theta$, then its corresponding patch

Table 2 Patch labeling by edge detection

ϕ	ϕ_{row}, ϕ_{col}	Type	Category
$\varphi < \theta$	–	Non-edge	–
$\varphi = \theta$	$\phi_{row} = \theta$	Edge	Horizontal
$\varphi = \theta$	$\phi_{col} = \theta$	Edge	Vertical
$\varphi = \theta$	$\phi_{row} = \theta$ and $\phi_{col} = \theta$	Edge	Slope
$\varphi > \theta$	–	Edge	Complex

is labelled as non edge else labelled the patch as edged. This makes the searching of the patches having more information faster.

2.3 Patch classification

The similar patches of an input patch are directly searched from the training database. However, this scheme is inefficient and similar optimal patches may not be obtained. Hence, to find out the similar optimal patches, we use feature similarity index (FSIM) [53] instead of the Euclidean distance, since it fails to search the appropriate nearest neighbor patches in the manifold. FSIM is computed by phase congruency ($S_{PC}(x)$) and gradient ($S_G(x)$) based similarity.

Feature similarity index is computed by combining $S_{PC}(x)$ and $S_G(x)$ as

$$S_L(x) = [S_{PC}(x)]^\alpha . [S_G(x)]^\beta, \tag{10}$$

where α and β are parameters for adjusting relative importance of both the features. Range of the FSIM is 0 to 1. The FSIM of two similar patches is nearer to 1. The value of FSIM between two patches lies between 0 to 1 and higher the value of FSIM, the similar the patches are. Thus, optimal patches are computed by top k-nearest neighbor patches with respect to FSIM.

2.4 Collaborative optimal weight reconstruction

In this section, a collaborative weight reconstruction is used during the HR patch generation. Firstly, the weight is computed using least squarer technique. Further, another weight vector is generated using non-negative matrix factorization method. Thereafter, final weight vector is collaboratively constructed using LS and NMF technique.

2.4.1 Weight vector generated by LS method

After generating the patches from images, each testing patch is taken into account to generate an expected HR patch. For each input patch l_t^q of $L_t = \{l_t^q, q = 1, 2, 3, ...m\}$, k-nearest neighbor training patches are searched. Through least square (LS) method the weights related to k-nearest neighbor training patches are found by minimizing the local reconstruction error as

$$\varepsilon^q = \min \left\| l_t^q - \sum_{l_r^p \in \aleph_q} w_{qp} l_r^p \right\|^2, \tag{11}$$

where $\aleph_q$ is the neighbor of l_t^q in training set L_r and element w_{qp} of W_q is the weight for l_r^p, subject to two constraints $\sum_{l_r^p \in \aleph_q} w_{qp} = 1$ and $w_{qp} = 0$ for any $l_r^p \notin \aleph_q$.

Let us define a local Gram matrix G_q for l_t^q as

$$G_q = \left(l_t^q 1^T - \mathbf{L} \right)^T \left(l_t^q 1^T - \mathbf{L} \right), \tag{12}$$

where 1 is a column vector of ones and $\mathbf{L}$ is a $D \times K$ matrix with its columns being the neighbors of x_t^q. To form a K-dimensional weight vector W_q, each weight w_{qp} is reordered by the subscript p.

To solve an eigenvalue problem using the Lagrange theorem, the formulation is given by

$$\varepsilon = w^T G w, \tag{13}$$

where

$$w = \left(\frac{1}{2}\right)\lambda G^{-1}1, \tag{14}$$

and

$$\lambda = \frac{2}{1^T G^{-1}1}. \tag{15}$$

When G is singular, the result of the least squares problem for finding w_q does not have the unique solution. The constrained least squares problem has the following closed-form solution as:

$$w_q = \frac{G_q^{-1}1}{1^T G_q^{-1}1}. \tag{16}$$

Hence, the least square optimal weight vector is represented by w_l where w_q is the element.

2.4.2 Weight vector generated by NMF method

Apart from that another weight vector is generated by non-negative matrix factorization (NMF). According to non-negative matrix factorization the weight is generated by

$$X \approx FG^T \tag{17}$$

$$x_t^i \approx x_d^i w \tag{18}$$

The iterative solution for (17) is proved to converge to a local minimum of the Euclidean distance $\|X - Fw_n T\|^2$. The iterative solution consists of two multiplicative update rules, both for F and w_{ij}. In this case matrix F, formed by the actual LR patches in the dictionary, is fixed and no update rule is needed for it. But the weight of each patch can be updated by

$$w_{ij} \leftarrow w_{ij} \sqrt{\frac{(x_d^{i^T} x_d^i)_j^+ + \left[w^{i^T}(x_d^{i^T} x_d^i)^-\right]_j}{(x_d^{i^T} x_d^i)_j^- + \left[w^{i^T}(x_d^{i^T} x_d^i)^+\right]_j}}. \tag{19}$$

The final weight vector is represented as w_n, where w_{ij} is the element.

Thus, a collaborative algorithm is developed by combine weight generated by LS and the NMF to compute the optimal weight vector. The collaborative optimal reconstruction weight for the HR patch reconstruction is defined as

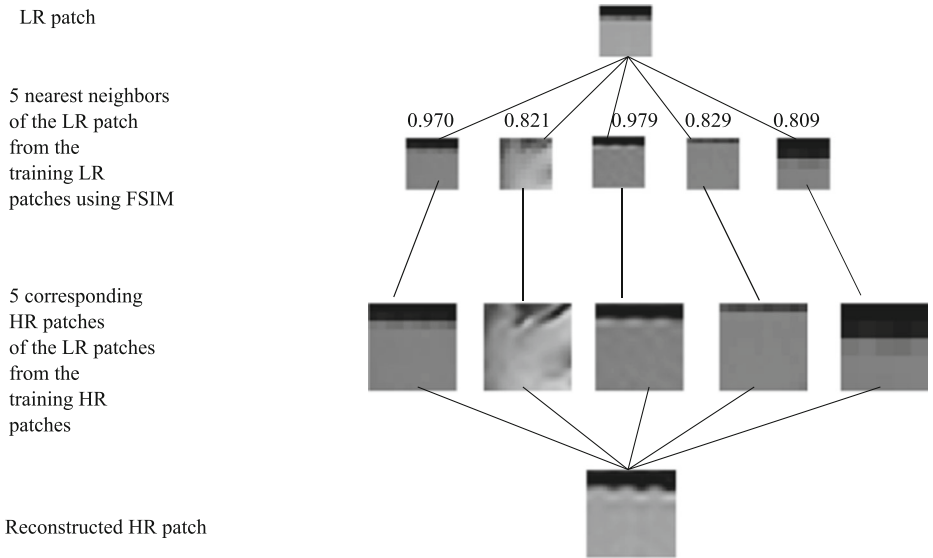$$\left| w = \frac{1}{2}w_q \cdot w_n + \frac{1}{4}(w_q + w_n) \right|, \tag{20}$$

where w_{ql} is the element of final optimal weight vector W.
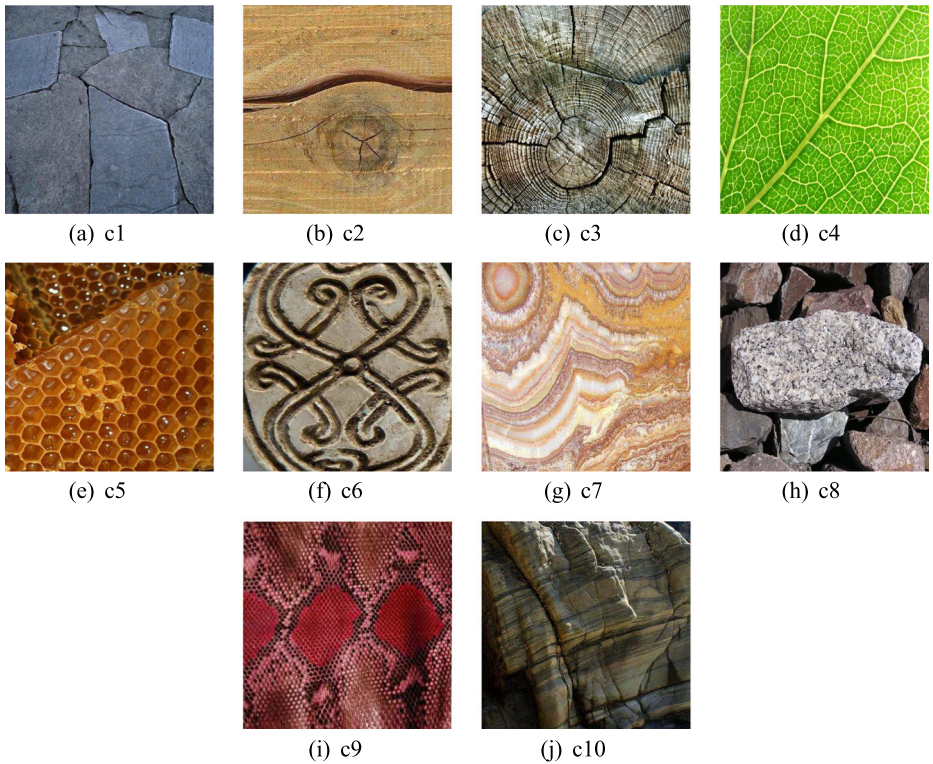
2.5 HR image reconstruction

As the manifold between LR-HR space is similar, the high-resolution output image patch h_t^q is computed as follows

$$h_t^q = \sum_{l_r^p \in \aleph_q} w_{ql} h_r^p + \overline{h_r^p}, \tag{21}$$

where $\overline{h_r^p}$ is the mean of the luminance and w_{ql} is the final reconstruction weight. The HR patch generation is shown in Fig. 3. To generate the output image, the overlapping patches $H_t = \{h_t^q\}_{q=1}^n$ is merged. The major factor that improves the performance of the

LR patch

5 nearest neighbors
of the LR patch
from the
training LR
patches using FSIM

0.970   0.821   0.979   0.829   0.809

5 corresponding
HR patches
of the LR patches
from the
training HR
patches

Reconstructed HR patch

Fig. 3 HR patch generation

(a) c1

(b) c2

(c) c3

(d) c4

(e) c5

(f) c6

(g) c7

(h) c8

(i) c9

(j) c10

Fig. 4 Testing color texture images

(a) g1　　　　　(b) g2　　　　　(c) g3　　　　　(d) g4

(e) g5　　　　　(f) g6　　　　　(g) g7　　　　　(h) g8

(i) g9　　　　　(j) g10
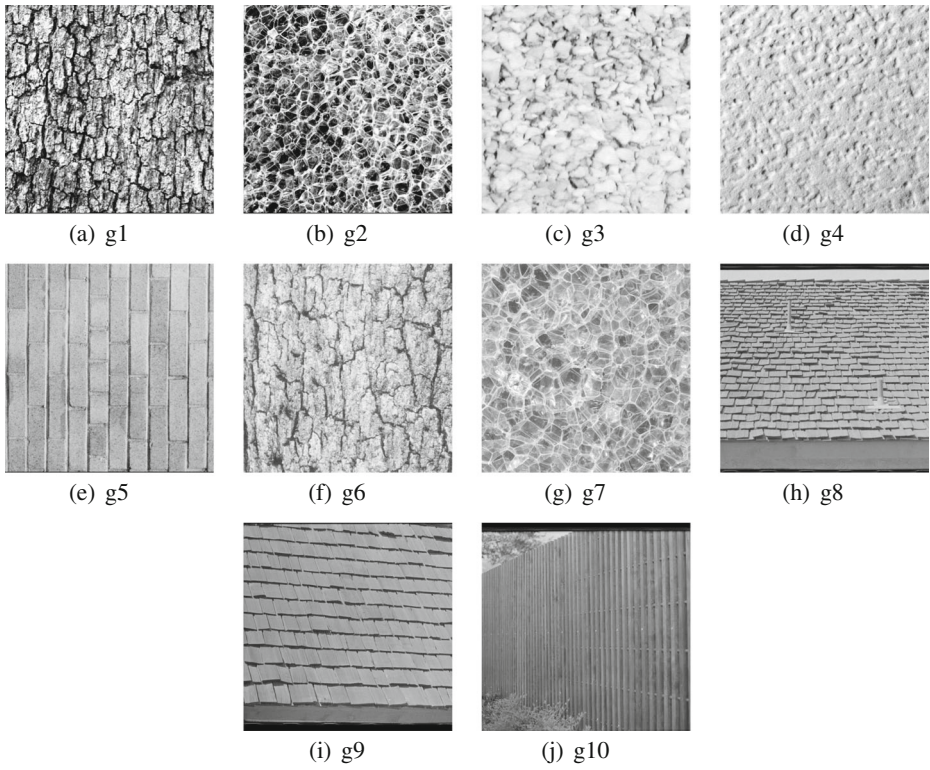
Fig. 5 Testing gray texture images

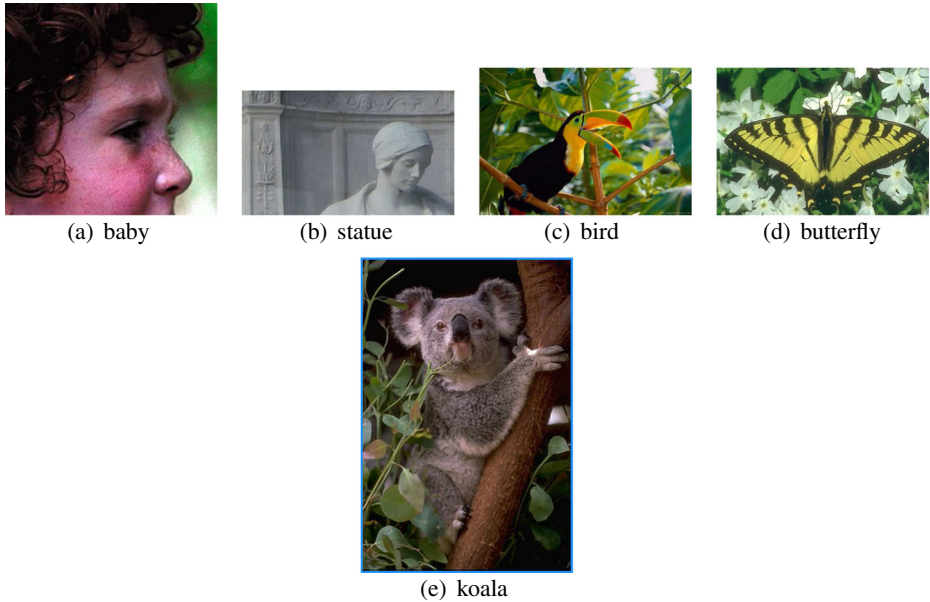(a) baby　　　　　(b) statue　　　　　(c) bird　　　　　(d) butterfly
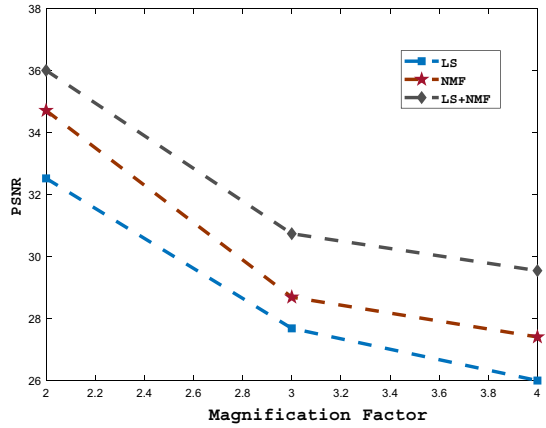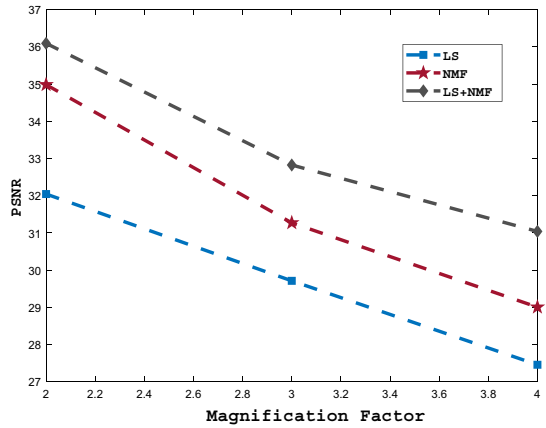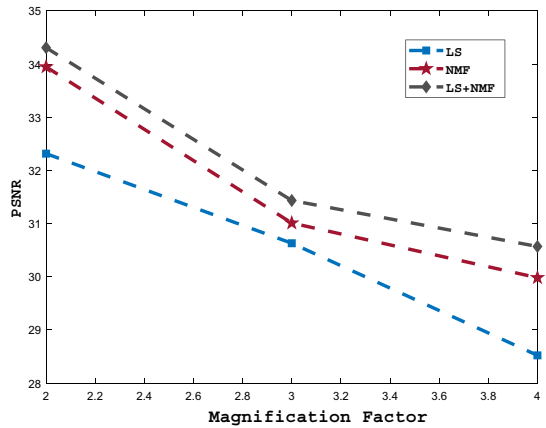
(e) koala

Fig. 6 Testing standard images

Fig. 7 PSNR evaluation with respect to various magnification factor (γ)
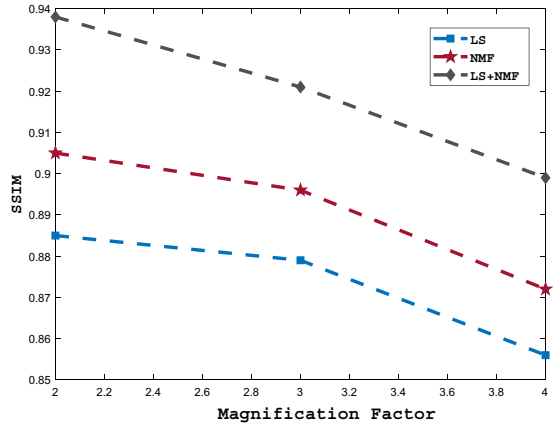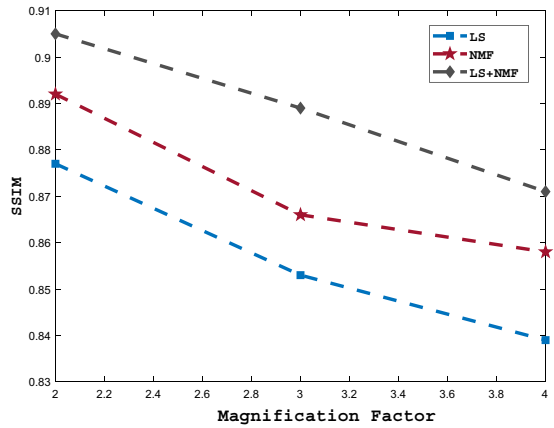

(a) Color image (c5).

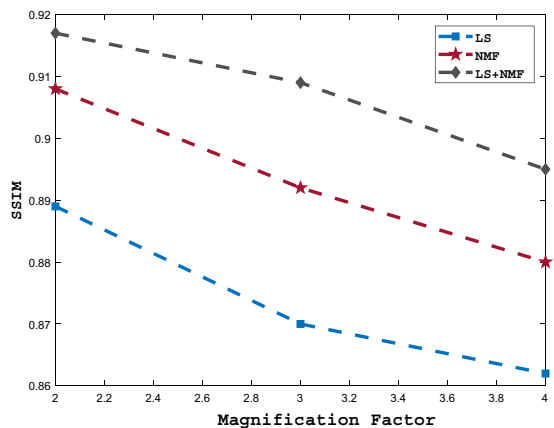(b) Gray image (g5).

(c) Standard image (butterfly).

Fig. 8 SSIM evaluation with respect to various magnification factor (γ)

(a) Color image (c5).

(b) Gray image (g5).

(c) Standard image (butterfly).

Table 3 PSNR of color texture image

Image	Patch size	Bicubic	EBSR [20]	SRNE [9]	NeedFS [7]	SCSR [46]	Proposed
1	**5**	23.542	24.689	25.981	26.879	28.199	**29.673**
	7	23.921	24.902	26.210	27.135	28.557	**30.020**
	9	24.322	25.162	26.765	27.687	28.873	**30.432**
2	**5**	26.571	27.021	28.399	29.128	30.199	**31.318**
	7	26.998	27.583	28.825	29.651	30.527	**31.764**
	9	27.216	28.017	29.210	29.983	30.938	**31.989**
3	**5**	24.412	25.513	26.882	27.436	28.529	**30.658**
	7	24.784	26.183	27.753	28.738	29.785	**30.993**
	9	25.338	26.953	28.081	29.098	30.128	**31.376**
4	**5**	23.114	24.537	25.521	26.467	27.783	**28.794**
	7	23.447	24.875	25.989	26.768	27.946	**29.065**
	9	23.978	25.369	26.377	27.407	28.517	**29.652**
5	**5**	25.561	26.714	27.684	28.317	29.843	**30.736**
	7	25.853	26.926	27.939	28.593	30.085	**31.161**
	9	26.329	27.418	28.112	28.846	30.511	**31.418**
6	**5**	27.452	28.581	29.739	30.283	31.629	**32.739**
	7	27.705	28.843	29.947	30.639	31.996	**33.105**
	9	28.111	29.167	30.257	30.973	32.261	**33.308**
7	**5**	25.765	26.841	27.929	28.585	29.374	**30.442**
	7	25.915	27.048	28.371	28.821	29.699	**30.585**
	9	26.421	27.322	28.626	29.018	29.951	**30.937**
8	**5**	24.643	25.629	26.751	27.579	28.777	**29.862**
	7	24.891	25.898	26.947	27.992	29.006	**30.235**
	9	25.235	26.366	27.551	28.311	29.628	**30.666**
9	**5**	27.121	28.440	29.612	30.745	31.593	**32.540**
	7	27.564	28.761	29.989	30.999	31.898	**32.798**
	9	27.860	28.999	30.115	31.333	32.047	**33.009**
10	**5**	25.519	26.111	27.413	28.176	28.577	**29.487**
	7	25.881	26.581	27.712	28.454	28.811	**29.888**
	9	26.110	26.889	28.001	28.891	29.218	**30.319**

The results of our proposed method are highlighted in bold

reconstruction image are neighborhood preservation between patches and optimal reconstruction weight. Hence, this paper mainly focuses on the feature selection, neighborhood patch search by similarity measures and the collaborative reconstruction weight. Finally, the reconstructed image in luminance channel has been combined with the interpolated chromatic channel. Thereafter, the YCbCr image is converted to RGB channel for final HR image reconstruction.

3 Experimental results

3.1 Experimental set up

In this paper, we validate our algorithm with various texture images collected from https://www.robots.ox.ac.uk/ vgg/data/dtd/ and http://sipi.usc.edu/database/database.php?volume=textures

Table 4 PSNR of gray texture image

Image	Patch size	Bicubic	EBSR [20]	SRNE [9]	NeedFS [7]	SCSR [46]	Proposed
1	**5**	25.908	26.839	27.692	28.759	30.199	**31.549**
	7	26.452	27.109	27.937	29.185	30.512	**31.792**
	9	26.891	27.688	28.318	29.512	30.877	**31.999**
2	**5**	22.999	24.176	25.521	26.479	27.698	**28.798**
	7	23.189	24.438	25.839	26.938	27.963	**29.067**
	9	23.569	24.850	26.089	27.279	28.352	**29.839**
3	**5**	24.068	25.371	26.247	27.614	28.895	**30.261**
	7	24.741	25.682	26.637	27.915	29.140	**30.592**
	9	25.122	25.931	26.951	28.311	29.583	**30.817**
4	**5**	22.890	23.902	25.021	26.316	27.555	**28.823**
	7	23.249	24.539	25.381	26.693	27.831	**29.261**
	9	23.795	24.906	25.794	26.967	28.205	**29.638**
5	**5**	27.496	28.628	29.713	30.649	31.782	**32.825**
	7	27.825	28.943	29.986	30.827	31.906	**33.184**
	9	28.219	29.28	30.362	31.271	32.299	**33.469**
6	**5**	24.067	25.103	26.409	27.498	28.749	**29.836**
	7	24.563	25.528	26.889	27.736	29.004	**30.261**
	9	24.998	25.937	27.141	28.103	29.486	**30.519**
7	**5**	26.892	27.818	28.925	30.026	31.281	**32.323**
	7	27.111	28.306	29.397	30.417	31.677	**32.745**
	9	27.789	28.777	29.829	30.748	31.901	**32.969**
8	**5**	25.335	26.499	27.671	28.557	29.757	**30.941**
	7	25.874	26.705	27.899	28.812	30.101	**31.289**
	9	26.543	26.909	28.381	29.285	30.421	**31.523**
9	**5**	23.447	24.613	25.641	26.712	27.903	**29.111**
	7	23.854	24.882	25.944	26.959	28.214	**29.731**
	9	24.111	25.260	26.279	27.428	28.653	**30.374**
10	**5**	25.241	26.417	27.578	28.539	29.721	**30.893**
	7	25.679	26.692	27.811	28.740	29.917	**31.254**
	9	25.888	26.916	28.179	28.957	30.318	**31.493**

The results of our proposed method are highlighted in bold

[43]. In addition, some standard images used in Matlab tool have been considered for the experiment. To conduct the experiment, LR image is produced from the original HR image by 5×5 Gaussian blur with a down-sampling factor 3. Both color and gray texture images are taken into account as shown in Figs. 4 and 5, respectively. Further, the scheme is validated on standard images as shown in Fig. 6. As human eyes has different sensitivity to change in illumination rather than chromatic component, the color image for the experiment is transformed from RGB to $YCbCr$ channel. Moreover, RGB component is not very compatible for image representation. Hence, the proposed algorithm executed on the Y component of the $YCbCr$ channel. The performance of the proposed scheme has been evaluated and a comparison has been made with different existing schemes. The existing competent schemes are Bicubic, EBSR [20], SRNE [9], NEVPM [17], NeedFS [7] and

Table 5 SSIM of color texture image

Image	Patch size	Bicubic	EBSR [20]	SRNE [9]	NeedFS [7]	SCSR [46]	Proposed
1	**5**	0.805	0.826	0.842	0.869	0.887	**0.904**
	7	0.813	0.839	0.855	0.878	0.895	**0.917**
	9	0.825	0.847	0.869	0.885	0.906	**0.929**
2	**5**	0.851	0.866	0.887	0.899	0.910	**0.924**
	7	0.863	0.873	0.896	0.909	0.922	**0.933**
	9	0.877	0.881	0.904	0.917	0.935	**0.941**
3	**5**	0.813	0.830	0.857	0.879	0.891	**0.907**
	7	0.822	0.839	0.869	0.888	0.903	**0.913**
	9	0.834	0.847	0.876	0.896	0.911	**0.926**
4	**5**	0.789	0.811	0.826	0.840	0.856	**0.871**
	7	0.799	0.824	0.834	0.849	0.867	**0.882**
	9	0.813	0.835	0.847	0.862	0.874	**0.991**
5	**5**	0.835	0.852	0.879	0.898	0.910	**0.921**
	7	0.842	0.861	0.888	0.909	0.921	**0.935**
	9	0.855	0.874	0.894	0.916	0.933	**0.941**
6	**5**	0.861	0.877	0.889	0.900	0.917	**0.939**
	7	0.873	0.883	0.896	0.909	0.925	**0.944**
	9	0.881	0.890	0.904	0.918	0.932	**0.951**
7	**5**	0.886	0.899	0.905	0.917	0.925	**0.932**
	7	0.893	0.906	0.911	0.923	0.932	**0.941**
	9	0.901	0.914	0.919	0.930	0.941	**0.950**
8	**5**	0.858	0.872	0.888	0.897	0.918	**0.929**
	7	0.863	0.878	0.894	0.904	0.926	**0.934**
	9	0.870	0.886	0.901	0.913	0.935	**0.942**
9	**5**	0.884	0.896	0.913	0.931	0.947	**0.959**
	7	0.890	0.904	0.921	0.939	0.952	**0.965**
	9	0.899	0.911	0.930	0.945	0.960	**0.971**
10	**5**	0.845	0.860	0.875	0.888	0.900	**0.927**
	7	0.853	0.868	0.882	0.896	0.909	**0.936**
	9	0.862	0.875	0.890	0.905	0.917	**0.944**

The results of our proposed method are highlighted in bold

SCSR [46]. To access the quality of the image, two commonly used performance measures are employed i.e., Peak Signal-to-Noise Ratio (PSNR) and Structural Similarity Index (SSIM) [42] to evaluate the sensitivity of the noise and structural similarity between the reconstructed image and ground truth image respectively.

3.2 Experimental results and discussion

3.2.1 Performance evaluation with varying magnification factor (γ)

In this section, we validate the proposed approach with respect to various magnification factor. In this approach, magnification factors are 2,3 and 4. Figures 7 and 8 show PSNR evaluation and SSIM evaluation with various magnification factor. From the given

Table 6 SSIM of gray texture image

Image	Patch size	Bicubic	EBSR [20]	SRNE [9]	NeedFS [7]	SCSR [46]	Proposed
1	**5**	0.815	0.829	0.841	0.859	0.872	**0.889**
	7	0.829	0.834	0.857	0.870	0.886	**0.895**
	9	0.837	0.845	0.865	0.882	0.897	**0.910**
2	**5**	0.769	0.781	0.805	0.829	0.841	**0.853**
	7	0.777	0.794	0.816	0.838	0.852	**0.866**
	9	0.799	0.808	0.827	0.845	0.865	**0.874**
3	**5**	0.794	0.812	0.823	0.839	0.851	**0.867**
	7	0.809	0.825	0.831	0.848	0.863	**0.875**
	9	0.818	0.835	0.844	0.856	0.871	**0.888**
4	**5**	0.730	0.748	0.760	0.781	0.799	**0.815**
	7	0.743	0.757	0.777	0.793	0.811	**0.829**
	9	0.755	0.769	0.788	0.809	0.823	**0.837**
5	**5**	0.827	0.841	0.853	0.865	0.879	**0.889**
	7	0.834	0.852	0.862	0.876	0.885	**0.896**
	9	0.845	0.866	0.871	0.883	0.893	**0.903**
6	**5**	0.856	0.869	0.881	0.893	0.907	**0.921**
	7	0.868	0.880	0.893	0.905	0.916	**0.934**
	9	0.877	0.893	0.901	0.911	0.929	**0.944**
7	**5**	0.809	0.820	0.835	0.852	0.868	**0.883**
	7	0.816	0.829	0.847	0.861	0.879	**0.891**
	9	0.823	0.837	0.856	0.874	0.892	**0.902**
8	**5**	0.819	0.831	0.849	0.865	0.879	**0.893**
	7	0.827	0.840	0.857	0.877	0.888	**0.905**
	9	0.835	0.852	0.869	0.884	0.901	**0.918**
9	**5**	0.802	0.819	0.831	0.849	0.867	**0.879**
	7	0.814	0.828	0.843	0.856	0.875	**0.886**
	9	0.821	0.837	0.856	0.868	0.888	**0.905**
10	**5**	0.877	0.891	0.909	0.918	0.930	**0.941**
	7	0.884	0.901	0.913	0.925	0.939	**0.950**
	9	0.890	0.910	0.921	0.933	0.945	**0.961**

The results of our proposed method are highlighted in bold

graph, it is observed that the quality is gradually decreasing according to the increase in magnification size. Hence, we consider 3 as the suitable factor for the experiment.

3.2.2 Performance evaluation with varying patch size (t)

The performance measures are computed with different patch sizes i.e., 5, 7, and 9. Tables 3 and 4 list the PSNR values of color and gray texture images respectively, whereas Tables 5 and 6 record the SSIM values for the color and gray respectively. Tables 7 and 8 show the PSNR and SSIM results for few standard images. It observed that the proposed method performs better than other existing methods on color texture, gray texture images and standard images. Further, it may be noticed that the larger the patch size, the better is the PSNR and SSIM values.

Table 7 PSNR of standard image

Image	Patch size	Bicubic	EBSR [20]	SRNE [9]	NeedFS [13]	SCSR [46]	Proposed
Statue	**5**	30.149	30.432	30.975	31.469	32.222	**32.599**
	7	30.786	30.981	31.996	32.149	32.642	**32.898**
	9	31.450	31.666	32.305	32.517	33.117	**33.325**
Koala	**5**	30.039	30.275	30.581	30.858	31.439	**31.689**
	7	30.631	30.894	30.955	31.102	31.784	**31.903**
	9	31.207	31.431	31.627	31.901	32.211	**32.437**
Butterfly	**5**	30.108	30.369	30.629	30.871	31.105	**31.433**
	7	30.755	30.930	30.894	31.009	31.582	**31.820**
	9	31.083	31.305	31.498	31.674	31.898	**32.105**
Head	**5**	31.777	32.263	32.402	33.361	33.611	**33.817**
	7	31.913	33.556	32.811	33.689	33.902	**34.026**
	9	32.218	33.989	33.405	34.210	34.205	**34.298**
Bird	**5**	32.157	32.672	33.912	34.133	34.394	**34.540**
	7	32.731	32.947	34.211	34.572	34.814	**34.968**
	9	33.018	33.316	34.426	34.748	35.008	**35.126**

The results of our proposed method are highlighted in bold

3.2.3 Performance evaluation by neighborhood preservation rate

In this section, neighborhood preservation rate is considered as another criterion to evaluate the efficacy of the proposed feature selection. Firstly, a group of LR patches have been selected randomly from the testing patch set. Then for each LR patch, the k-nearest neighbor patches have been considered from the test set. Prior to this, the corresponding k-nearest neighbor HR patches are identified from the HR patches. Comparing the number

Table 8 SSIM of standard image

Image	Patch size	Bicubic	EBSR [20]	SRNE [9]	NeedFS [7]	SCSR [46]	Proposed
Statue	**5**	0.799	0.823	0.882	0.891	0.907	**0.914**
	7	0.821	0.837	0.889	0.905	0.916	**0.920**
	9	0.842	0.845	0.896	0.917	0.925	**0.929**
Koala	**5**	0.762	0.781	0.839	0.852	0.893	**0.905**
	7	0.772	0.796	0.846	0.866	0.907	**0.918**
	9	0.789	0.816	0.857	0.879	0.919	**0.928**
Butterfly	**5**	0.795	0.853	0.870	0.883	0.898	**0.909**
	7	0.821	0.863	0.876	0.891	0.903	**0.917**
	9	0.836	0.880	0.884	0.901	0.911	**0.925**
Head	**5**	0.742	0.802	0.805	0.811	0.821	**0.844**
	7	0.759	0.817	0.814	0.820	0.829	**0.867**
	9	0.766	0.822	0.826	0.829	0.835	**0.882**
Bird	**5**	0.804	0.827	0.835	0.856	0.874	**0.895**
	7	0.810	0.831	0.844	0.865	0.872	**0.911**
	9	0.823	0.845	0.859	0.877	0.881	**0.925**

The results of our proposed method are highlighted in bold
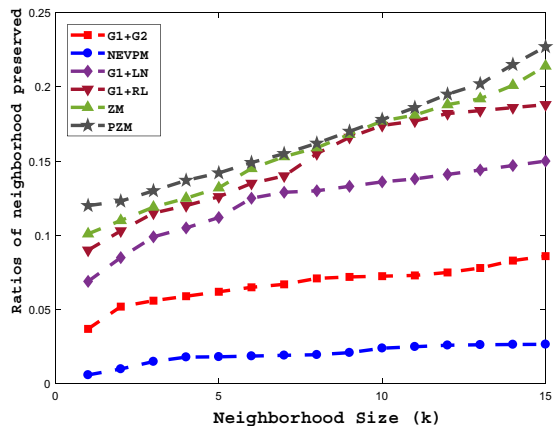
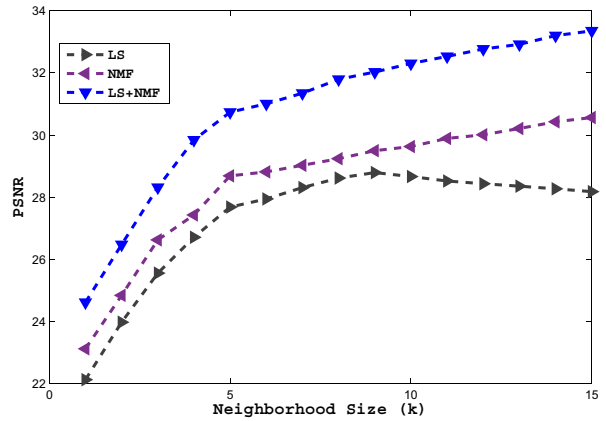**Fig. 9** Neighborhood preservation of test image
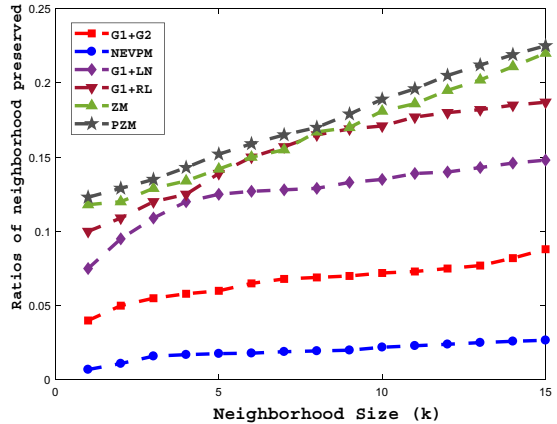
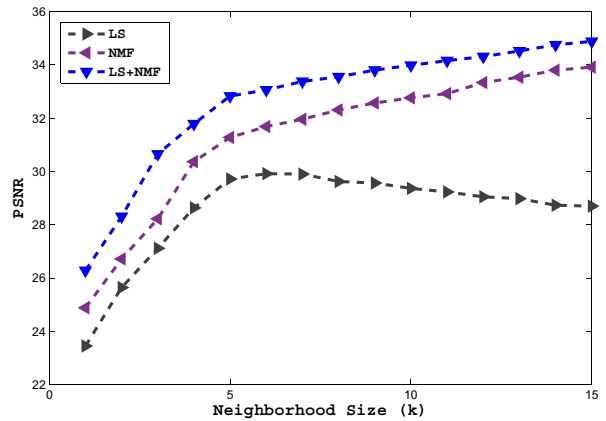(a) Color image (c5).
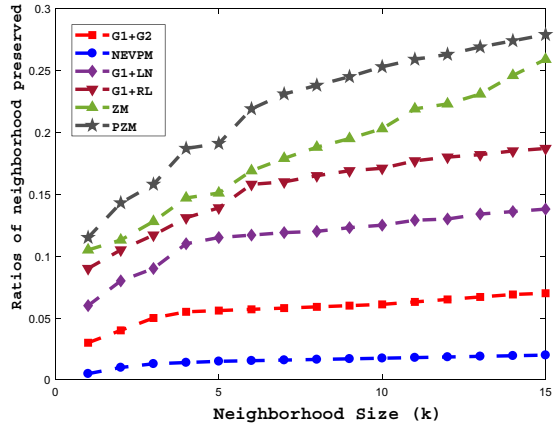
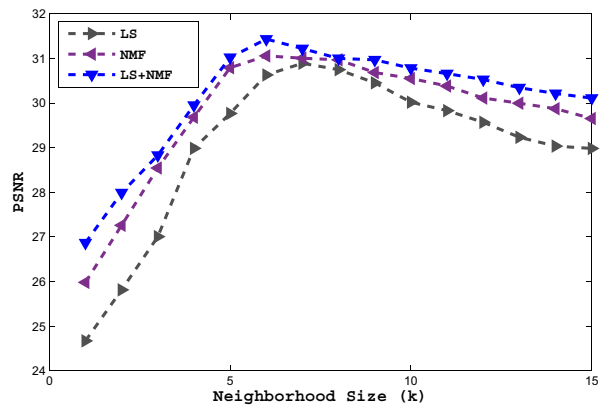(b) Gray image (g5).

(c) Standard image (butterfly).

Fig. 10 PSNR evaluation with respect to various neighborhood size (*k*)
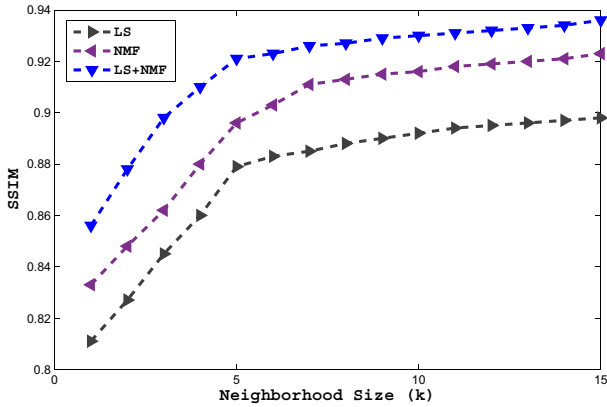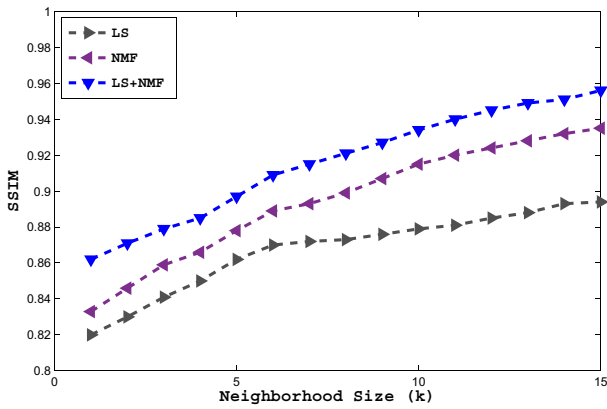

(a) Color image (c5).

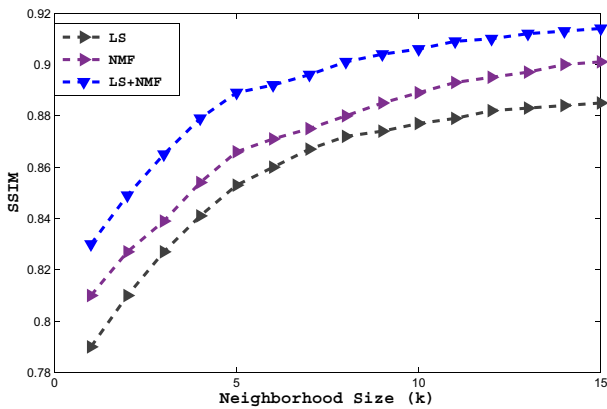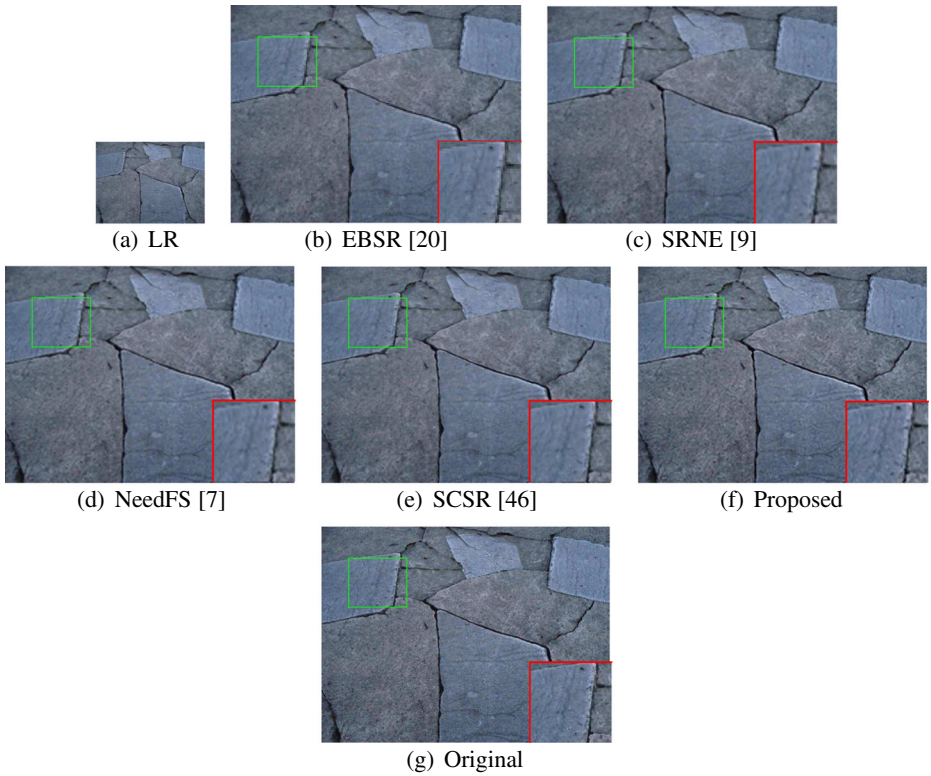(b) Gray image (g5).

(c) Standard image (butterfly).

(a) Color image (c5).

(b) Gray image (g5).

(c) Standard image (butterfly).
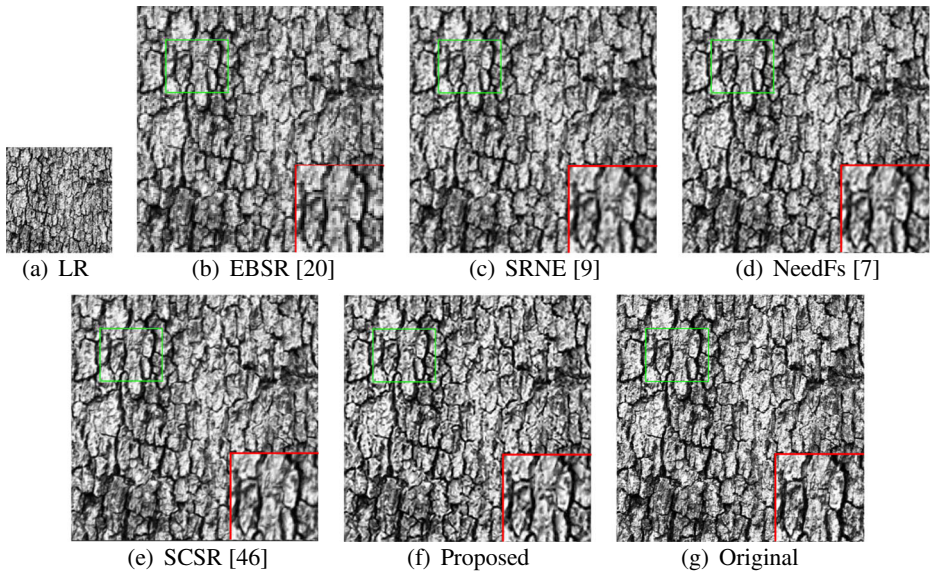
Fig. 11 SSIM evaluation with respect to various neighborhood size (*k*)

(a) LR　　　　(b) EBSR [20]　　　　(c) SRNE [9]

(d) NeedFS [7]　　　　(e) SCSR [46]　　　　(f) Proposed

(g) Original

Fig. 12 Comparison of SR results with (3×) magnification for $c1$ image

(a) LR　　(b) EBSR [20]　　(c) SRNE [9]　　(d) NeedFs [7]

(e) SCSR [46]　　　　(f) Proposed　　　　(g) Original
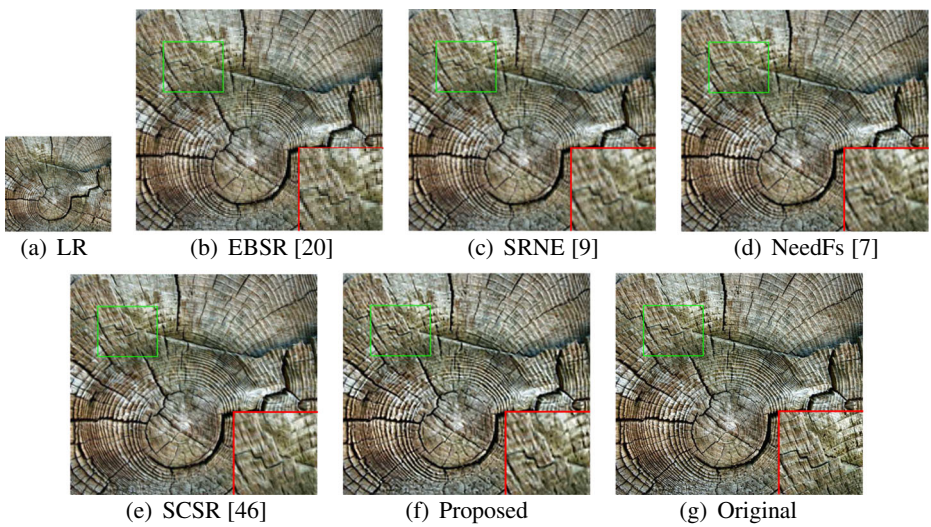
Fig. 13 Comparison of SR results with (3×) magnification for $c3$ image

(a) LR (b) EBSR [20] (c) SRNE [9] (d) NeedFs [7]

(e) SCSR [46] (f) Proposed (g) Original

Fig. 14 Comparison of SR results with (3×) magnification for $g1$ image

of corresponding HR patches of the k-nearest neighbor of LR patches, the neighborhood preservation rate is obtained.

In this section, we have performed the comparison between LR and HR patch with different features used in the state-of-the-art schemes. In SRNE [9] method, first gradient and second gradient are used as features, whereas in NeedFS [7] a combination of first-order gradient and norm luminance are considered. NESRRL [32] considered first gradient

(a) LR (b) EBSR [20] (c) SRNE [9] (d) NeedFs [7]

(e) SCSR [46] (f) Proposed (g) Original
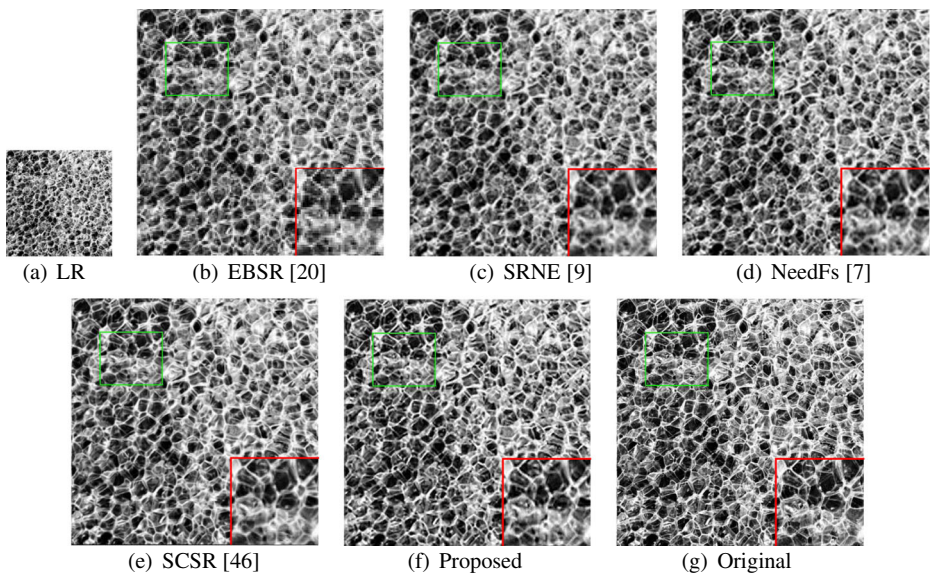
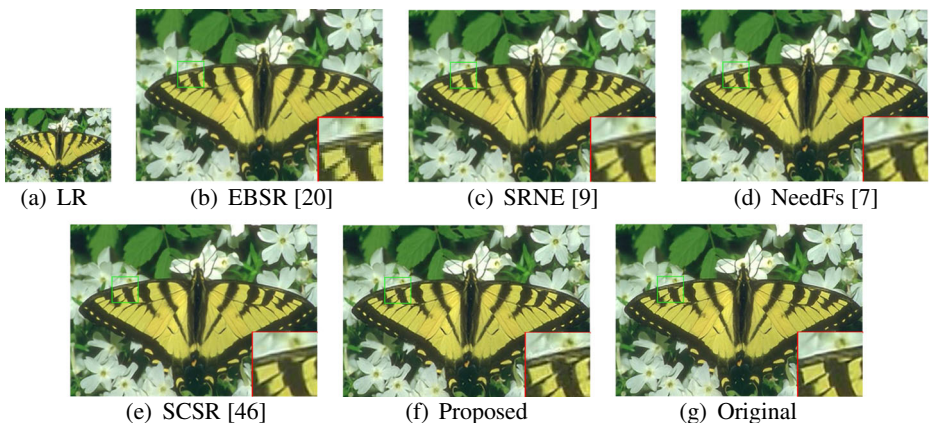**Fig. 15** Comparison of SR results with (3×) magnification for $g2$ image
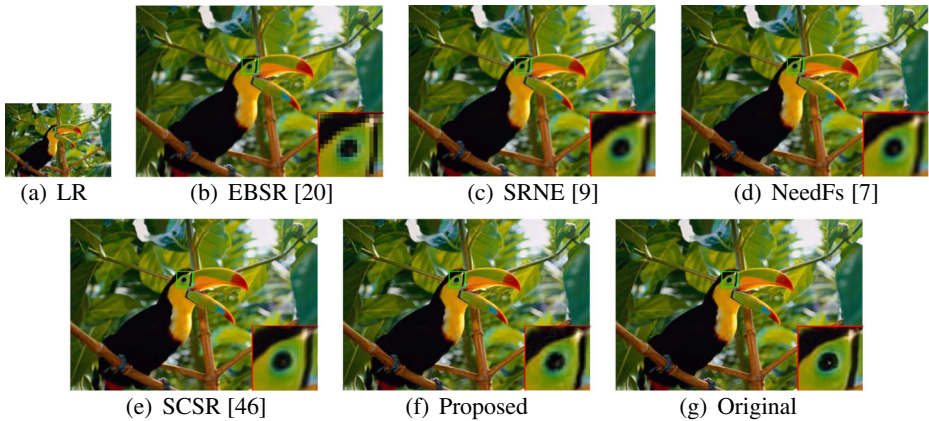
Fig. 16 Comparison of SR results with (3×) magnification for *bird* image

and residual luminance as the feature vector to generate the expected HR image. More-over, to verify the advantage of PZM over ZM, we have validated with [34]. In this work, we have used PZM for feature generation. Here, we randomly consider 1800 LR patches, and out of which 300 patches are used as testing LR patches. Then, we have evaluated the neighborhood preservation for 3 magnification with different neighborhood size.

The neighborhood preservation rate obtained by the existing schemes with respect to different neighborhood size are shown in Fig. 9. It can be observed that the proposed scheme achieves better results as compared to the existing schemes by means of neighborhood preservation rate due to better feature vector.

3.2.4 Performance evaluation varying with neighborhood size (k)

It has been observed that the neighborhood size has significant impact on the performance of the model. Hence, in this experiment the neighborhood size is varied between 1 to 15 and the corresponding PSNR and SSIM results for color, gray texture images and standard

Fig. 17 Comparison of SR results with (3×) magnification for *butterfly* image

images are shown in Figs. 10 and 11 respectively. It may be seen that the proposed scheme achieves better PSNR and SSIM results for neighborhood size between 5 to 8. Further, the visual performance comparisons for three different category of images are shown in Figs. 12, 13, 14, 15, 16 and 17. From these figures, it may be observed that the propose scheme yields better visualization results than other state-of-the-art schemes.

4 Conclusion

In this paper, a new framework for learning based super resolution has been proposed for texture image. Pseudo Zernike moments are utilized for the feature selection. Moreover, FSIM is used for patch classification during neighbor embedding. Subsequently, a collaborative optimal reconstruction weight is computed to HR patch generation. Optimal reconstruction weight is defined by the combination of least square error and non-negative factorization matrix. The experimental results on texture and standard images demonstrate that the proposed scheme achieves better results than other competent schemes. In future, we intent to explore our method on different images like areal image, medical image, video surveillance, etc. In addition, other feature generation schemes could be investigated as the potential alternatives to PZM.

References

1. Ahn IJ, Nam WH (2016) Texture enhancement via high-resolution style transfer for single-image super-resolution. arXiv:1612.00085
2. Baker S, Kanade T (2002) Limits on super-resolution and how to break them. IEEE Trans Pattern Anal Mach Intell 24(9):1167–1183. https://doi.org/10.1109/TPAMI.2002.1033210
3. Begin I, Ferrie FP (2004) Blind super-resolution using a learning-based approach. In: 2004 International conference on pattern recognition, pp 85–89. https://doi.org/10.1109/ICPR.2004.1334046
4. Bevilacqua M, Roumy A, Guillemot C, Morel MLA (2013) Super-resolution using neighbor embedding of back-projection residuals. In: 18th International conference on digital signal processing, pp 1–8. https://doi.org/10.1109/ICDSP.2013.6622796
5. Cao M, Gan Z, Zhu X (2012) Super-resolution algorithm through neighbor embedding with new feature selection and example training. In: 2012 IEEE International conference on signal processing, vol 2, pp 825–828. https://doi.org/10.1109/ICoSP.2012.6491708
6. Chan TM, Zhang J (2006) An improved super-resolution with manifold learning and histogram matching. In: 2006 International conference on advances in biometrics, pp 756–762. https://doi.org/10.1007/11608288_101
7. Chan TM, Zhang J, Pu J, Huang H (2009) Neighbor embedding based super-resolution algorithm through edge detection and feature selection. Pattern Recogn Lett 30(5):494–502. https://doi.org/10.1016/j.patrec.2008.11.008
8. Chang X, Yang Y (2017) Semisupervised feature analysis by mining correlations among multiple tasks. IEEE Transactions on Neural Networks and Learning Systems 28(10):2294–2305. https://doi.org/10.1109/TNNLS.2016.2582746
9. Chang H, Yeung DY, Xiong Y (2004) Super-resolution through neighbor embedding. In: 2004 IEEE Computer society conference on computer vision and pattern recognition, vol 1, pp 275–28. https://doi.org/10.1109/CVPR.2004.1315043
10. Chang X, Ma Z, Lin M, Yang Y, Hauptmann A (2017) Feature interaction augmented sparse learning for fast kinect motion detection. IEEE Trans Image Process 26(8):3911–3920. https://doi.org/10.1109/TIP.2017.2708506

11. Chang X, Ma Z, Yang Y, Zeng Z, Hauptmann AG (2017) Bi-level semantic representation analysis for multimedia event detection. IEEE Trans Cybern 47(5):1180–1197. https://doi.org/10.1109/TCYB.2016.2539546

12. Chang X, Yu YL, Yang Y, Xing EP (2017) Semantic pooling for complex event analysis in untrimmed videos. IEEE Trans Pattern Anal Mach Intell 39(8):1617–1632. https://doi.org/10.1109/TPAMI.2016.2608901

13. Chen X, Qi C (2014) Nonlinear neighbor embedding for single image super-resolution via kernel mapping. Signal Process 94:6–22. https://doi.org/10.1016/j.sigpro.2013.06.016

14. Chong CW, Raveendran P, Mukundan R (2003) The scale invariants of pseudo-Zernike moments. Pattern Anal Appl 6(3):176–184. https://doi.org/10.1007/s10044-002-0183-5

15. Cruz C, Mehta R, Katkovnik V, Egiazarian K (2017) Single image super-resolution based on Wiener filter in similarity domain. arXiv:1704.04126

16. Dong W, Zhang L, Shi G, Li X (2013) Nonlocally centralized sparse representation for image restoration. IEEE Trans Image Process 22(4):1620–1630. https://doi.org/10.1109/TIP.2012.2235847

17. Fan W, Yeung DY (2007) Image hallucination using neighbor embedding over visual primitive manifolds. In: 2007 IEEE Conference on computer vision and pattern recognition, pp 1–7. https://doi.org/10.1109/CVPR.2007.383001

18. Farsiu S, Robinson D, Elad M, Milanfar P (2004) Advances and challenges in super-resolution. Int J Imaging Syst Technol 14(2):47–57. https://doi.org/10.1002/ima.20007

19. Freeman WT, Pasztor EC, Carmichael OT (2000) Learning low-level vision. Int J Comput Vis 40(1):25–47. https://doi.org/10.1023/A:1026501619075

20. Freeman WT, Jones TR, Pasztor EC (2002) Example-based super-resolution. IEEE Comput Graph Appl 22(2):56–65. https://doi.org/10.1109/38.988747

21. Gao X, Wang Q, Li X, Tao D, Zhang K (2011) Zernike-moment-based image super resolution. IEEE Trans Image Process 20(10):2738–2747. https://doi.org/10.1109/TIP.2011.2134859

22. Gao X, Zhang K, Tao D, Li X (2012) Joint learning for single-image super-resolution via a coupled constraint. IEEE Trans Image Process 21(2):469–480. https://doi.org/10.1109/TIP.2011.2161482

23. Gerchberg R (1974) Super-resolution through error energy reduction. Optica Acta: Int J Opt 21(9):709–720. https://doi.org/10.1080/713818946

24. Guo K, Yang X, Lin W, Zhang R, Yu S (2012) Learning-based super-resolution method with a combining of both global and local constraints. IET Image Process 6(4):337–344. 10.1049/iet-ipr.2010.0430

25. HaCohen Y, Fattal R, Lischinski D (2010) Image upsampling via texture hallucination. In: 2010 IEEE International conference on computational photography, pp 1–8. https://doi.org/10.1109/ICCPHOT.2010.5585097

26. Jiang J, Ma X, Cai Z, Hu R (2015) Sparse support regression for image super-resolution. IEEE Photon J 7(5):1–11. https://doi.org/10.1109/JPHOT.2015.2484287

27. Kanan HR, Salkhordeh S (2016) Rotation invariant multi-frame image super resolution reconstruction using pseudo Zernike moments. Signal Process 118:103–114. https://doi.org/10.1016/j.sigpro.2015.05.015

28. Kim SP, Bose NK, Valenzuela HM (1990) Recursive reconstruction of high resolution image from noisy undersampled multiframes. IEEE Trans Acoust Speech Signal Process 38(6):1013–1027. https://doi.org/10.1109/29.56062

29. Li X, Orchard MT (2001) New edge-directed interpolation. IEEE Trans Image Process 10(10):1521–1527. https://doi.org/10.1109/83.951537

30. Lin Z, Shum HY (2004) Fundamental limits of reconstruction-based superresolution algorithms under local translation. IEEE Trans Pattern Anal Mach Intell 26(1):83–97. https://doi.org/10.1109/TPAMI.2004.1261081

31. Liu L, Huang W, Wang C (2017) Texture image prior for SAR image super resolution based on total variation regularization using split bregman iteration. Int J Remote Sens 38(20):5673–5687. https://doi.org/10.1080/01431161.2017.1346325

32. Mishra D, Majhi B, Sa PK (2014) Neighbor embedding based super-resolution using residual luminance. In: 2014 Annual IEEE India conference (INDICON), pp 1–6. https://doi.org/10.1109/INDICON.2014.7030659

33. Mishra D, Majhi B, Sa PK, Dash R (2016) Development of robust neighbor embedding based super-resolution scheme. Neurocomputing 202:49–66. https://doi.org/10.1016/j.neucom.2016.04.013

34. Mishra D, Majhi B, Sa PK (2017) Improved feature selection for neighbor embedding super-resolution using Zernike moments. In: Proceedings of international conference on computer vision and image processing, pp 13–24. https://doi.org/10.1007/978-981-10-2107-7_2

35. Nasrollahi K, Moeslund TB (2014) Super-resolution: a comprehensive survey. Mach Vis Appl 25(6):1423–1468. https://doi.org/10.1007/s00138-014-0623-4

36. Park SC, Park MK, Kang MG (2003) Super-resolution image reconstruction: a technical overview. IEEE Signal Process Mag 20(3):21–36. https://doi.org/10.1109/MSP.2003.1203207
37. Patanavijit V (2009) Super-resolution reconstruction and its future research direction. AU J Technol 12(3):149–163
38. Rajan D, Chaudhuri S, Joshi MV (2003) Multi-objective super resolution: concepts and examples. IEEE Signal Process Mag 20(3):49–61. https://doi.org/10.1109/MSP.2003.1203209
39. Sajjadi MS, Schölkopf B., Hirsch M (2016) Enhancenet: single image super-resolution through automated texture synthesis. arXiv:1612.07919
40. Sun J, Zheng NN, Tao H, Shum HY (2003) Image hallucination with primal sketch priors. In: 2003 IEEE Computer society conference on computer vision and pattern recognition, vol 2, pp 29–36. https://doi.org/10.1109/CVPR.2003.1211539
41. Tsai RY, Huang TS (1984) Multiframe image restoration and registration. Adv Comput Vis Image Process 1(2):317–339
42. Wang Z, Bovik AC, Sheikh HR, Simoncelli EP (2004) Image quality assessment: from error visibility to structural similarity. IEEE Trans Image Process 13(4):600–612. https://doi.org/10.1109/TIP.2003.819861
43. Weber AG (1997) The USC-SIPI image database. http://sipi.usc.edu/database/database.php?volume=textures
44. Wei LY, Lefebvre S, Kwatra V, Turk G (2009) State of the art in example-based texture synthesis. In: Eurographics 2009, State of the Art Report, EG-STAR
45. Yang J, Huang T (2010) Image super-resolution: historical overview and future challenges. In: Milanfar P (ed) Super-Resolution imaging, chap. 1. CRC Press, pp 1–24. ISBN: 9781439819302
46. Yang J, Wright J, Huang TS, Ma Y (2010) Image super-resolution via sparse representation. IEEE Trans Image Process 19(11):2861–2873. https://doi.org/10.1109/TIP.2010.2050625
47. Yang S, Wang Z, Zhang L, Wang M (2014) Dual-geometric neighbor embedding for image super resolution with sparse tensor. IEEE Trans Image Process 23(7):2793–2803. https://doi.org/10.1109/TIP.2014.2319742
48. Yoo SB, Choi K, Jeon YW, Ra JB (2016) Texture enhancement for improving single-image super-resolution performance. Signal Process Image Commun 46:29–39. https://doi.org/10.1016/j.image.2016.04.007
49. Zachevsky I, Zeevi YY (2014) Single-image superresolution of natural stochastic textures based on fractional brownian motion. IEEE Trans Image Process 23(5):2096–2108. https://doi.org/10.1109/TIP.2014.2312284
50. Zeyde R, Elad M, Protter M (2010) On single image scale-up using sparse-representations. In: Proceedings of the 7th international conference on curves and surfaces, vol 6920, pp 711–730. https://doi.org/10.1007/978-3-642-27413-8_47
51. Zhang L, Wu X (2006) An edge-guided image interpolation algorithm via directional filtering and data fusion. IEEE Trans Image Process 15(8):2226–2238. https://doi.org/10.1109/TIP.2006.877407
52. Zhang K, Gao X, Li X, Tao D (2011) Partially supervised neighbor embedding for example-based image super-resolution. IEEE J Selected Topics Signal Process 5(2):230–239. https://doi.org/10.1109/JSTSP.2010.2048606
53. Zhang L, Zhang D, Mou X, Zhang D (2011) FSIM: a feature similarity index for image quality assessment. IEEE Trans Image Process 20(8):2378–2386. https://doi.org/10.1109/TIP.2011.2109730
54. Zhang K, Gao X, Tao D, Li X (2012) Single image super-resolution with non-local means and steering kernel regression. IEEE Trans Image Process 21(11):4544–4556. https://doi.org/10.1109/TIP.2012.2208977

Deepasikha Mishra is an Assistant Professor at the Department of Computer Science & Engineering, Vellore Institute of Technology, Amaravati, India. Her research interest includes the domain of image processing, computer vision, and pattern recognition. She is currently pursuing doctoral research at National Institute of Technology Rourkela, India. She also served as resource associate for research project by Defence Research and Development Organization, India.

Banshidhar Majhi is a Professor with the Department of Computer Science and Engineering, National Institute of Technology Rourkela, India. He is presently serving as Director of Indian Institute of Information Technology Design & Manufacturing Kancheepuram, India. He has successfully executed various Research and Development projects being funded by agencies such as MHRD, ISRO, DRDO, and DeitY. He has authored hundreds of articles in reputed journals and conferences. His current research interests include image processing, computer vision, biometric security, and pattern recognition. He has been conferred with prestigious awards and honors for his contribution towards scientific research and academic excellence.

Sambit Bakshi is currently with Centre for Computer Vision and Pattern Recognition of National Institute of Technology Rourkela, India. He also serves as Assistant Professor in Department of Computer Science & Engineering of the institute. He earned his PhD degree in Computer Science & Engineering in 2015. He currently serves as associate editor of International Journal of Biometrics (2013 -), IEEE Access (2016 -), Innovations in Systems and Software Engineering : A NASA Journal (2016 -), and Plos One (2017 -). He is technical committee member of IEEE Computer Society Technical Committee on Pattern Analysis and Machine Intelligence. He received the prestigious Innovative Student Projects Award 2011 from Indian National Academy of Engineering (INAE) for his master's thesis. He has more than 50 publications in journals, reports, conferences.

Arun Kumar Sangaiah has received his Master of Engineering (ME) degree in Computer Science and Engineering from the Government College of Engineering, Tirunelveli, Anna University, India. He had received his Doctor of Philosophy (PhD) degree in Computer Science and Engineering from the VIT University, Vellore, India. He is presently working as an Associate Professor in School of Computer Science and Engineering, VIT University, India. His area of interest includes software engineering, computational intelligence, wireless networks, bio-informatics, and embedded systems. He has authored more than 100 publications in different journals and conference of national and international repute. His current research work includes global software development, wireless ad hoc and sensor networks, machine learning, cognitive networks and advances in mobile computing and communications. Also, he was registered a one Indian patent in the area of Computational Intelligence. Besides, Prof. Sangaiah is responsible for Editorial Board member / Associate Editor of various international journals.

Pankaj Kumar Sa received the Ph.D. degree in computer science from NIT Rourkela in 2010. He is currently an Assistant Professor with the CSE Department, NIT Rourkela. He has authored or co-authored a number of research articles in various journals, conferences, and book chapters. His research interests include computer vision, biometrics, and visual surveillance. He is a member of the CSI. He has co-investigated some R&D projects funded by SERB, PXE, DeitY, and ISRO. He has been conferred with various prestigious awards and honors. Apart from research and teaching, he is also actively involved with the automation of NIT Rourkela, where he conceptualizes and engineers the automation process.